AIAA SciTech Forum
9 - 13 January 2017, Grapevine, Texas
58th AIAA/ASCE/AHS/ASC Structures, Structural Dynamics, and Materials Conference

10.2514/6.2017-0182

Check for updates

Multi-Discipline Modeling of Complete Hypersonic Vehicles Using CFD Surrogates

Emily R. Dreyer*[1], Ryan J. Klock†[2], Benjamin J. Grier‡[1],
Jack J. McNamara§[1], and Carlos E.S. Cesnik¶[2]

[1]The Ohio State University, Columbus, OH, 43210, USA
[2]University of Michigan, Ann Arbor, MI, 48109, USA

Downloaded by UNIVERSITY OF MICHIGAN on April 5, 2018 | http://arc.aiaa.org | DOI: 10.2514/6.2017-0182

Accurate and efficient estimation of aerothermodynamic loads is a fundamental challenge for multi-disciplinary modeling and analysis of ultra high-speed vehicles. This study focuses on this issue by assessing the accuracy and studying the impact of combined theoretical and data-driven models over a broad operational space. A computational fluid dynamics (CFD) enriched piston theory (EPT) approach is benchmarked against both CFD and a basic engineering approach from a combined shock-expansion and third order piston theory (SEP) model. In the EPT approach, the enrichment is supplied by Kriging interpolation over a set of steady-state Reynolds-Averaged Navier-Stokes (RANS) solutions. The first part of this study focuses on offline assessment of the accuracy of the reduced models relative CFD. The second part carries out online comparisons of the impact the reduced models have on the dynamics of a free flying vehicle. The EPT approach is found to yield improved agreement with CFD relative to SEP for offline predictions. Furthermore, the use of EPT for online loads prediction of a free flying vehicle significantly shifts open loop vehicle response, with SEP predicting larger inclination and roll angle changes than EPT. Both aft body flow interactions and modeling errors are discussed as potential causes.

Nomenclature

a	Speed of sound
A	Grid cell area
C_D	Drag coefficient
C_L	Lift coefficient
D	Grid dimension
E_{max}	Maximum absolute error
E_{mean}	Mean absolute error
H	Enthalpy
L_B	Roll moment
M	Mach number
N	Number of grid points
p	Pressure
$\mathrm{p_{ang}}, \mathrm{q_{ang}}, \mathrm{r_{ang}}$	Angular velocites
Pr	Prandtl number
Q	Heat flux
r	Grid refinement factor
R	Gas constant for air

*Graduate Research Assistant, Department of Mechanical & Aerospace Engineering, Student Member AIAA, dreyer.40@osu.edu
†Graduate Research Assistant, Department of Aerospace Engineering, Student Member AIAA, rjklock@umich.edu
‡Post-Doctoral Researcher, Department of Mechanical & Aerospace Engineering, grier.44@osu.edu
§Associate Professor, Department of Mechanical & Aerospace Engineering, Associate Fellow AIAA, mcnamara.190@osu.edu
¶Professor, Department of Aerospace Engineering, Fellow AIAA, cesnik@umich.edu

Copyright © 2017 by E. Dreyer, R. Klock, B. Grier, J. McNamara, and C. Cesnik. Published by the American Institute of Aeronautics and Astronautics, Inc., with permission.

Re_x	Reynolds number
St	Stanton number
T	Temperature
U	Fluid velocity
v_n	Normal velocity
x, y, z	Physical coordinates
y^+	Inner scaling for wall-normal direction
$Z(x, y, z, t)$	Position of structural surface
α	angle-of-attack
β	Sideslip angle
γ	Specific heat ratio
δ	Boundary layer thickness
Θ	Flow deflection angle
μ	Shock wave angle
ν	Prandtl-Meyer function
ρ	Density
σ	Standard deviation
ϕ, θ, ψ	Euler angles

Subscripts

∞	Freestream
0	Total condition
aw	Adiabatic wall
fin	Quantity for a fin only
loc	Local
max	Maximum
min	Minimum
n	Normal
ref	Reference or freestream quantity
uns	Unsteady
w	At the wall or surface

Downloaded by UNIVERSITY OF MICHIGAN on April 5, 2018 | http://arc.aiaa.org | DOI: 10.2514/6.2017-0182

I. Introduction

THE United States Air Force (USAF) seeks advanced hypersonic vehicle systems[1] that maintain precision and reliability in extreme environments. An inherent challenge is accounting for the associated strong, dynamic fluid-structural interactions in the early stages of system design and development, and throughout broad simulation of the vehicle over its operational life. This requires multi-disciplinary computational frameworks that accurately and expediently predict the vehicle response.[1]

There is a significant degree of uncertainty associated with multi-disciplinary modeling of high speed systems and, currently, limited ability to alleviate this uncertainty through experimental testing. Due to the infeasibility of ground tests, the lack of available flight test data, and the extreme cost of obtaining either, the primary means of analysis must be computational. In the context of aerothermodynamic loads prediction, computational fluid dynamics (CFD) can provide a high accuracy solution for complex flows (*e.g.* 3-D effects, inviscid-viscous interactions, impinging shocks, turbulence). However, such an approach is not yet amenable for online loads prediction in multi-disciplinary design and simulation frameworks. Classical engineering-level approximations are expedient, but cannot provide sufficient accuracy for all required conditions. These general issues have motivated a significant number of studies on model reduction

techniques that can harness the capabilities of high-fidelity flow modeling tools, while remaining computationally tractable.[2–10]

One promising approach in high speed flow fields, where the fluid-structural coupling is typically quasi-steady, is to generate a surrogate model based on a combination of steady-state CFD and theoretical fluid models.[7–10] Here, the steady-state CFD captures complex flow features, while the theoretical models are used to correct the steady-state loads for feedback effects due to dynamic fluid-structural and fluid-thermal coupling. In order to further reduce the computational effort, the steady-state CFD is replaced with a data-driven model, such as Kriging interpolation. This approach has been examined in the context of 2-D and 3-D lifting surfaces and panels, and found to yield excellent agreement with unsteady CFD at a computational cost comparable to engineering-level analyses.[7–10] Zettl *et al.*[11] demonstrated the use of Kriging interpolation to predict steady-state pressure for axisymmetric configurations over broad multi-dimensional parameter spaces. The Kriging models more accurately captured the complex 3-D flow features when compared to a shock-expansion model, and the computational cost was comparable to the shock-expansion model. However, to date, this approach has not yet been assessed in time-varying simulations of full-scale vehicle systems.

The objective of this study is to develop and assess the CFD surrogate approach for application to hypersonic vehicles operating on representative trajectories. This is accomplished through construction and assessment of a CFD surrogate model by benchmarking against unsteady CFD, as well as exercising the surrogate model in a coupled hypersonic vehicle flight dynamics framework.

II. Methodology

First, the CFD model and vehicle configuration are detailed. Next, two variants on local piston theory are discussed. In the first model, local flow quantities are approximated using Kriging interpolation of steady-state CFD solutions. The second approach obtains the local flow quantities from a theoretical shock-expansion model. Convergence and error assessment of the Kriging interpolation for the steady-state CFD are discussed. Lastly, details are provided on the multi-disciplinary framework used for predicting the free flight of hypersonic vehicles.

A. CFD Model and Configuration

The NASA Langley unstructured grid compressible flow solver, FUN3D,[12] is used to generate both the steady-state Reynolds-Averaged Navier-Stokes (RANS) flow solutions needed to construct and validate the Kriging models and to provide unsteady flow solutions for quantifying interpolation accuracy. FUN3D uses a node-based finite volume discretization. The Spalart-Allmaras turbulence model[13] is used throughout, and real gas effects are neglected.

Shown in Fig. 1 are the grid and geometry for the finned axisymmetric hypersonic vehicle configuration considered. The hybrid grid consists of both pyramid and tetrahedral elements. The viscous layer was generated using anisotropic cells with an estimated $y^+ < 2$. This configuration, which includes four all-movable fins, was developed by Witeof and Neergaard[14] using the Preliminary Aerothermal Structural Simulation (PASS) code suite.[15] Table 2 summarizes basic properties of the configuration, and Table 3 lists the full range of assumed operational parameters for this configuration. Note that deflection of the fins is beyond the mesh deformation scheme in FUN3D, and requires advanced overset mesh capabilities. The incorporation of overset meshes is currently in progress, but is not part of this study. Hence, all CFD computations in this paper are restricted to zero fin deflection relative to the vehicle.

Table 2. Vehicle properties for a fully fueled configuration.

Body length (m)	3.56
Body diameter (m)	0.36
Wingspan (m)	0.82
Center of gravity location (m)	(2.09, 0, 0)
Mass (kg)	375

Downloaded by UNIVERSITY OF MICHIGAN on April 5, 2018 | http://arc.aiaa.org | DOI: 10.2514/6.2017-0182

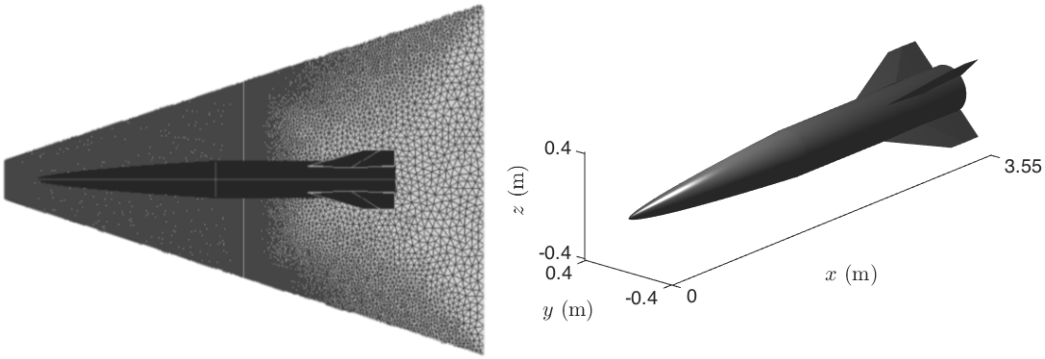

Figure 1. Computational domain and geometry for a finned axisymmetric hypersonic vehicle configuration.

Downloaded by UNIVERSITY OF MICHIGAN on April 5, 2018 | http://arc.aiaa.org | DOI: 10.2514/6.2017-0182

Table 3. Vehicle parameter space.

2	Mach	7
0	Altitude (kft)	85
-30	$\alpha(^\circ)$	30
-30	$\beta(^\circ)$	30
217	T_w (K)	3700

Grid convergence for the unstructured domain is examined using a series of systematically refined grids using a constant refinement factor over the entire domain while also maintaining the same grid quality (skewness), aspect ratio, and growth rate. The grid refinement factor, r, is defined as:[16]

$$r = \left(\frac{N_1}{N_2}\right)^{1/D} \tag{1}$$

where N_1 is the number of points in the fine mesh, N_2 is the number of points in the coarse mesh, and D is the grid dimension. A grid refinement factor of 1.5 is used.

The mesh convergence is conducted for two freestream conditions of Mach 6.0 at 85 kft altitude for angle-of-attack and sideslip angle both equal to 0° and 30°, respectively. These two conditions correspond to total inclination angles relative to the freestream flow of 0° and 42.4°. Lift and drag coefficients are used to determine convergence where percent error is measured against the finest grid and reported as an average of the error at the two flight conditions. Results of the study are summarized in Table 4. The fine grid is considered converged with percent errors for C_L and C_D of 1.30% and 0.00%, respectively.

Table 4. Grid convergence as determined from variation of C_L and C_D as a function of grid resolution.

		Error (%)	
	Points	C_L	C_D
Coarse	3.4M	259	34.0
Medium	5.1M	4.76	0.09
Fine	9.9M	1.30	0.00
Finest	35M	-	-

B. Surface Pressure Modeling

A potentially important feature for accurate loads prediction of hypersonic configurations is the ability to couple with vehicle and subsystem dynamics. Due to the high speed nature of the flow, it is assumed that the vehicle and/or subsystem dynamics are quasi-steady relative to the fluid dynamics. Thus, a local piston theory approach provides a reasonable model for the surface pressure.[17] Two different methods are used to compute the required local flow properties. The theoretical approach uses shock-expansion theory. This is denoted as the shock-expansion-piston theory (SEP) model. A refined approach is to use steady-state CFD to capture more complex flow characteristics compared to the shock-expansion solutions. Since online CFD is intractable for large parameter spaces and long time records, Kriging interpolation over a series of offline steady-state CFD solutions is used. This approach is denoted as CFD enriched piston theory (EPT). The following sections describe these different components in more detail. Note that a fundamental open issue is whether the improved fidelity by the CFD-based model is counteracted by the introduction of interpolation errors when considering online computations in a dynamical system.

1. *Local Piston Theory*

Consider the standard third order binomially expanded form of the exact piston pressure expression:[18]

$$p(x,y,z,t) = p_\infty + \gamma p_\infty \left\{ \frac{v_n}{a_\infty} + \frac{\gamma+1}{4}\left(\frac{v_n}{a_\infty}\right)^2 + \frac{\gamma+1}{12}\left(\frac{v_n}{a_\infty}\right)^3 \right\} \tag{2}$$

where

$$v_n = \dot{Z}(x,y,z,t) + U_\infty \left[Z^{'}(x,y,z,t) \right]. \tag{3}$$

where $\dot{Z}$ and $Z^{'}$ represent derivatives in time (t) and space (x) of the outer mold line, respectively.

The use of freestream quantities in Eqs. 2 & 3 is only valid for predominantly inviscid flow conditions where the local surface inclination and/or surface motion are sufficiently small and induce shock waves or expansion fans. In the presence of other complex flow features (*e.g.* 3-D effects, inviscid-viscous interactions, impinging shocks), the use of local flow quantities that spatially vary along the surface provides an improved approximation.[8,10,19] Thus, replacing all freestream quantities with local quantities:

$$p(x,y,z,t) = p_{loc} + \gamma p_{loc} \left\{ \frac{v_n}{a_{loc}} + \frac{\gamma+1}{4}\left(\frac{v_n}{a_{loc}}\right)^2 + \frac{\gamma+1}{12}\left(\frac{v_n}{a_{loc}}\right)^3 \right\} \tag{4}$$

where

$$v_n = \dot{Z}(x,y,z,t) + U_{loc} \left[Z^{'}(x,y,z,t) \right] \tag{5}$$

Equation 4 represents a perturbation from the local surface pressure due to surface motion. Furthermore, the second terms in Eqs. 3 and 5 represent the dependence of the pressure on surface inclination. Since piston theory is restricted to relatively small hypersonic similarity numbers,[18] this term often limits the applicability of piston theory. Local piston theory provides a convenient means to alleviate this issue by computing the local flow quantities for instantaneous surface inclination. In this case, p_{loc} inherently captures the dependency of surface pressure on surface inclination, and the spatial derivatives in Eq. 5 must be ignored, leaving:

$$v_n = \dot{Z}(x,y,z,t) \tag{6}$$

In this study, all surface inclinations due to vehicle dynamics are used to compute local flow quantities. Surface inclination changes at the fins due to fin actuation is also accounted for in the local flow quantities in the SEP model. Thus, the SEP model uses Eq. 6. As noted previously, this is not the case when using the Kriging interpolation for the EPT model, *i.e.* the steady-state CFD solutions are computed with the fins at zero angle-of-attack relative to the body. As a result, the EPT model must use:

$$v_n = \dot{Z}(x,y,z,t) + U_{loc}\alpha_{fin} \tag{7}$$

where α_{fin} is the local angle-of-attack of the fin relative to the body.

Downloaded by UNIVERSITY OF MICHIGAN on April 5, 2018 | http://arc.aiaa.org | DOI: 10.2514/6.2017-0182

Finally, note that the local speed of sound, a_{loc}, is a function of local temperature, $T_{loc}(x, y, z, t)$, and ideal gas constant, R:

$$a_{loc} = \sqrt{\gamma R T_{loc}(x, y, z, t)} \tag{8}$$

Since temperature is not constant through the boundary layer, the definition of a local condition for the temperature is not precisely defined. As piston theory is derived as an inviscid flow model, a logical choice is to define local temperature at the boundary layer edge. However, this requires *a priori* estimation of the boundary layer edge location in order to extract the temperature from a CFD solution. This location is approximated here using the equation for turbulent flows over a flat plate:[20]

$$\delta(x) = \frac{0.37x}{Re_x^{1/5}} \tag{9}$$

where Re_x is the local Reynolds number. It is assumed that the boundary layer edge is located $\delta(x)$ radially from the surface.

2. *Kriging Interpolation of Steady-State CFD*

Following the establishment of desired input parameters and appropriate bounds, the sample points for the Kriging interpolation are selected from a quasi-random set generated using a Halton sequence.[21] Here, each sample point corresponds to a combination of the parameters for which a steady-state RANS CFD solution is computed. To ensure the points sufficiently span the domain of the parameter space, the points used for model construction and validation are taken from the same Halton set. A total of $n + K$ points in the parameter space are computed, of which n are used for model construction, and K distinct points are used for evaluation. If further accuracy is desired, more sample responses are added and the process is repeated. In this study, $100 \leq n \leq 900$ and $K = 100$.

Three Kriging models are required for the surface pressure prediction. One for steady-state surface pressure, a second for local temperature at the boundary layer edge, and a third for local Mach number at the boundary layer edge. Note that the latter two are required for approximating a_{loc} and U_{loc}. Convergence is analyzed using the values required by local piston theory, which are p/p_{ref}, a_{loc}/a_{ref} predicted for the boundary layer edge of the full outer mold line (OML), and U_{loc}/U_{ref} predicted for the boundary layer edge of the fins only. Convergence of the models is quantified using L_1- and L_∞-norms, given by:

$$L_1 = \sum_{i=1}^{m} \left(\frac{1}{A_i}\right) \sum_{i=1}^{m} \left|\left(\text{MODEL}_i - \text{CFD}_i\right)\left(A_i\right)\right| \tag{10}$$

$$L_\infty = \text{Max}\left|\left(\text{MODEL}_i - \text{CFD}_i\right)\left(A_i\right)\right| \tag{11}$$

where m corresponds to the total number of data points in a test case. Note that large positive to negative variations in the surface distributions for a single prediction complicates the definition of an appropriate normalization quantity. Thus, only absolute error is used to assess convergence here. In Figs. 2 and 3 the Kriging models begin to exhibit convergence starting at 500 sample points for p/p_{ref}, and by 700 sample points for a_{loc}/a_{ref} and U_{loc}/U_{ref}.

Note that error in the U_{loc}/U_{ref} prediction is compounded since the U_{loc} calculation requires predictions from two surrogates: T_{loc} and M_{loc}. As the norms of a_{loc}/a_{ref} and U_{loc}/U_{ref} still exhibit slight downward trends, further convergence would be likely with the inclusion of more sample points. Furthermore, the relatively high L_∞-norms compared to the L_1-norms indicate that the Kriging interpolation is susceptible to large localized regions of error on the models. Target additional points may also alleviate this issue as well.

Finally, an issue with this Kriging approach is the potential for significant interpolation errors due to sparse sampling of the hypercube space. For the current axisymmetric configuration, preliminary testing indicated that inadequate sampling near the $\alpha = \beta = 0$ origin leads to asymmetric pressure distributions that produce non-zero roll moments and large roll rates if uncontrolled. This is mitigated by prescribing additional sample points at and around $\alpha = \beta = 0$. However, it is impractical to completely remove the interpolation errors. Thus a tolerance must be established in order to define adequate model accuracy. A preliminary tolerance is set here as the roll moment induced by 1 degree of fin rotation predicted by the

Downloaded by UNIVERSITY OF MICHIGAN on April 5, 2018 | http://arc.aiaa.org | DOI: 10.2514/6.2017-0182

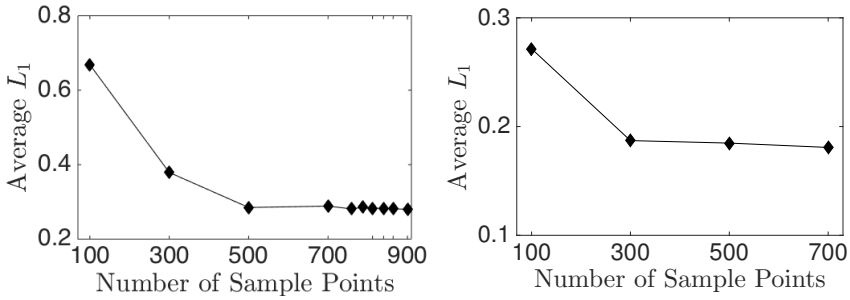

(a) p/p_{ref} for full OML (b) a_{loc}/a_{ref} for full OML

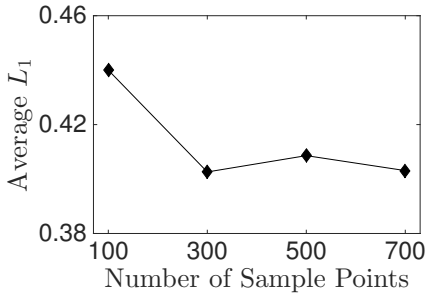

(c) U_{loc}/U_{ref} for fins only

Figure 2. Kriging interpolation convergence for average L_1-norm.

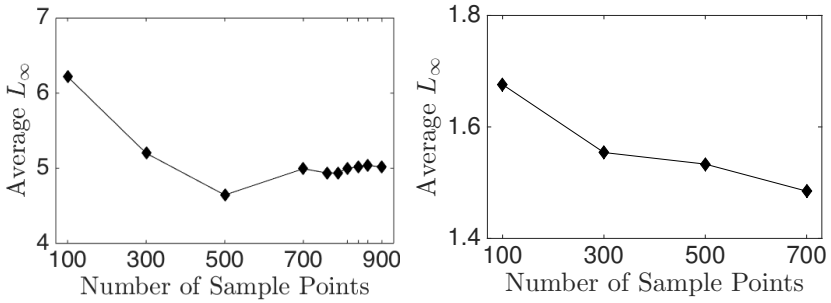

(a) p/p_{ref} for full OML (b) a_{loc}/a_{ref} for full OML

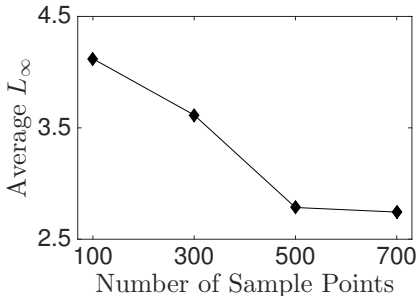

(c) U_{loc}/U_{ref} for fins only

Figure 3. Kriging interpolation convergence for average L_∞-norm.

SEP model. The roll moments produced by the Kriging model (KR) for $\alpha = \beta = 0$ and by the SEP model for 1 degree fin rotation are shown in Fig. 4. These results suggest that the constructed Kriging model has sufficiently small error when $\alpha = \beta = 0$.

Downloaded by UNIVERSITY OF MICHIGAN on April 5, 2018 | http://arc.aiaa.org | DOI: 10.2514/6.2017-0182

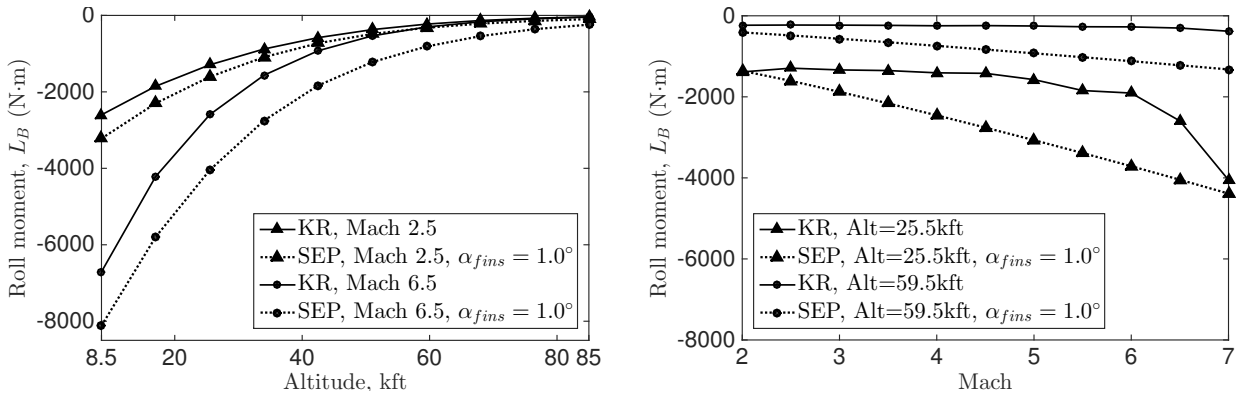

Figure 4. Roll moment predicted with KR versus altitude and Mach number at $\alpha = \beta = 0$ compared to roll moment induced by 1 degree of fin deflection predicted with SEP.

Downloaded by UNIVERSITY OF MICHIGAN on April 5, 2018 | http://arc.aiaa.org | DOI: 10.2514/6.2017-0182

3. *Shock-Expansion Model*

Oblique shock and Prandtl-Meyer wave relations form a basic model to determine the steady flow properties and forces for simple shapes in supersonic flow.[20] Here it is assumed that each planar panel of the vehicle is exposed to a steady, inviscid, supersonic flow at angle Θ, measured between the panel and the freestream flow. Depending on Θ, there are four possible solution types for determining post-wave conditions. These are: 1) detached shock, 2) oblique shock, 3) expansion fan, or 4) separated flow. For use in the local piston theory expression, the resulting flow properties from these solutions are specified as the local quantities used in Eq. 4.

A detached shock will occur when Θ is between 90° and $\Theta_{\max}$. defined by:

$$\Theta_{\max} = \tan^{-1}\left[\frac{2\cot(\mu_{\max}(M_1^2\sin^2\mu_{\max} - 1))}{M_1^2(\gamma + \cos(2\mu_{\max})) + 2}\right] \tag{12}$$

where $\mu_{\max}$ is the maximum attached shock wave angle, M_1 is the upstream Mach number, and γ is the specific heat ratio of air. Normal shock relations are used to compute the conditions post-shock, including the pressure ratio give by:

$$\frac{p_2}{p_1} = \frac{2\gamma M_{1_n}^2 - (\gamma - 1)}{\gamma + 1} \tag{13}$$

were M_{1_n} is the component of the upstream Mach number normal to the shock wave.[20] An oblique shock will occur for Θ between $\Theta_{\max}$ and 0°. Using the weak solution from the wave angle, μ, normal shock relations are again used to compute the post-shock conditions, with pressure ratio given by Eq. 13. The third flow type is expansion fan, which occurs when the flow is turned away from itself, meaning Θ is between 0° and the minimum deflections angle $\Theta_{\min}$, given by:

$$\Theta_{\min} = \nu(M_1) - \nu_{\min} \tag{14}$$

where ν is the Prandtl-Meyer function.[20] Assuming isentropic flow across an expansion fan, the pressure ratio is given by:[20]

$$\frac{p_2}{p_1} = \left[\frac{1 + \frac{\gamma-1}{2}M_1^2}{1 + \frac{\gamma-1}{2}M_2^2}\right]^{\frac{\gamma}{\gamma-1}}. \tag{15}$$

The final possible post-wave condition is separated flow, which occurs when Θ is less than Θ_{min}. In this case, the flow is turned through the minimum deflection angle. Accurate quantification of this flow is beyond the scope of this shock-expansion theory model. Thus, pressure, temperature, and density are assumed to be zero in these regions.

C. Vehicle Dynamics

All free flying vehicle responses are evaluated using the University of Michigan High-Speed Vehicle (UM/HSV) code, which provides a framework for aerodynamic, thermodynamic, and elastic interaction simulation of hypersonic vehicles using full and reduced order models.[22–24] The code includes six degree of freedom flight time simulation, high speed vehicle trim, and linear state matrix identification. A more detailed description of the aeroelastic solution methods is described by Klock and Cesnik.[22–24] The code is written in a modular format that allows for the removal, exchange, or isolation of entire components. This enables trade studies for models of varying fidelity.

III. Results and Discussion

Analysis of the aerodynamic modeling approaches is carried out by: 1) benchmarking the steady-state pressure models against steady-state CFD; 2) comparing the CFD enriched piston theory predictions with unsteady CFD; and 3) assessing the impact of the modeling approaches on free flying vehicle dynamics.

A. Steady-State Pressure Prediction

The quality of the reduced models for steady-state pressure is assessed by comparing with RANS CFD in terms of mean and maximum surface pressure, lift and drag coefficients, and spatial distribution of error.

1. *Mean Surface Pressure*

The L_1 error (Eq. 10) is compared to the mean normalized pressure for shock-expansion (SE), and Kriging interpolation (KR), in Fig. 5. The results are ordered by decreasing mean normalized CFD pressure. Although the mean normalized pressure from shock-expansion is relatively close to that from CFD, the shock-expansion model over predicts the mean normalized pressure for 100% of the evaluation cases. The consistently small L_1 error for Kriging interpolation indicates a significant improvement over the shock-expansion model. The difference is most apparent at high values of mean normalized pressure.

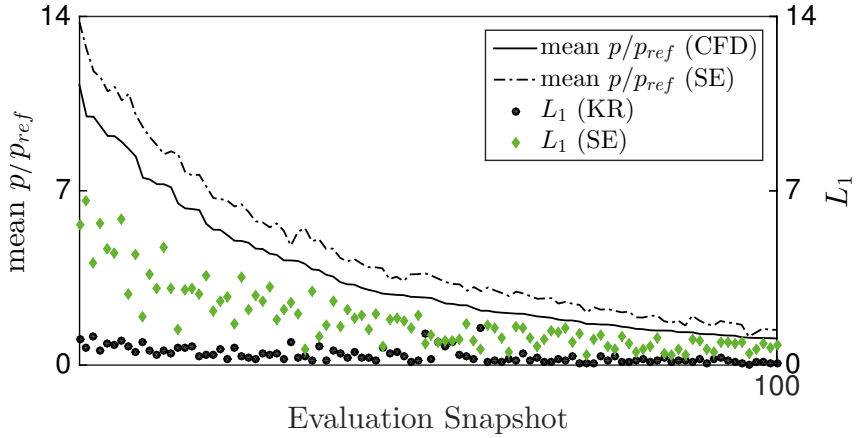

Figure 5. Mean p/p_{ref} and L_1.

2. *Maximum Surface Pressure*

Similar results are shown in Fig. 6 for the L_∞ error (Eq. 11) for KR and SE predictions relative to the maximum predicted CFD pressure. The results are ordered by decreasing maximum normalized CFD pressure. The shock-expansion model generally yields higher error than Kriging interpolation. The shock-expansion model also under predicts the maximum normalized pressure for 100% of the evaluation cases, yet some of the shock-expansion errors exceed the maximum normalized pressure predicted by shock-expansion. Note

Downloaded by UNIVERSITY OF MICHIGAN on April 5, 2018 | http://arc.aiaa.org | DOI: 10.2514/6.2017-0182

that all of the 12 Kriging cases where the maximum error is greater than the maximum pressure are near or at the edge of the parameter space.

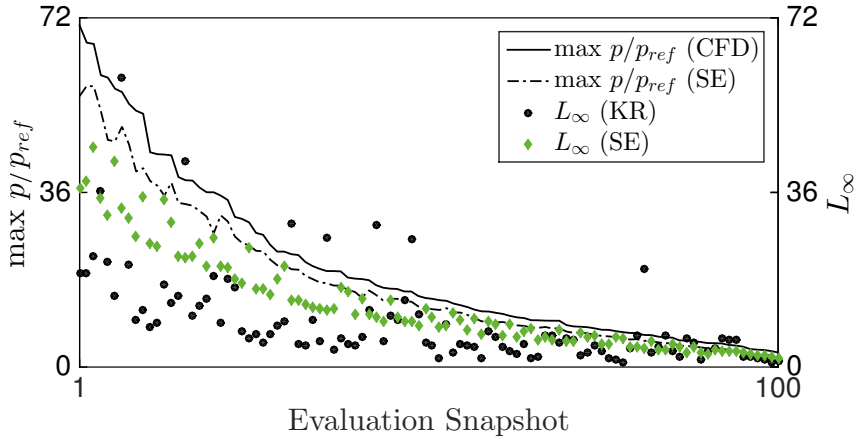

Figure 6. Maximum p/p_{ref} and L_∞.

3. *Aerodynamic Coefficients*

The accuracy of the absolute values of lift and drag coefficients for CFD are compared to the absolute errors of the models in Figs. 7(a) and 7(b). Consistent with the previous results, Kriging interpolation generally provides significant improvement over the shock-expansion model and is at worst comparable in error. The largest errors relative to the aerodynamic coefficients occur at lower absolute values, corresponding to cases with small incidence angles.

4. *Spatial Distribution of Error*

In order to gain further insight, consider the mean and maximum absolute error (Eqs. 10 & 11) and standard deviation of Kriging interpolation for normalized surface pressure shown in Fig. 8. Both are computed over the $K = 100$ evaluation points. For comparison, similar plots are presented in Fig. 9 for shock-expansion. Figs. 8 and 9 present four views of the axisymmetric vehicle.

Kriging performs significantly better than shock-expansion, which is highlighted by the large standard deviations across the entire vehicle in Fig. 9(b). For both models, the greatest errors are localized to the nose of the vehicle, the leading edges of the fins, and the regions between fins where there are significant flow interactions. This is expected as stagnation regions and areas with strong 3-D effects are difficult to accurately model. Note that shock-expansion performs significantly worse near the rear of the vehicle where complex flow interactions dominate the solution.

The CFD prediction for surface pressure distribution for the specific Kriging interpolation test case with maximum error is shown in Fig. 10. The corresponding pressure and absolute value in error for the Kriging and shock-expansion model predictions are shown in Fig. 11. This case is located near the edge of the parameter space at 85 kft and Mach 6.5, and a total inclination angle of 16.8°. While the shock-expansion model cannot account for the complex flow interactions and 3-D effects, such complexities are approximated reasonably well in general using Kriging interpolation.

B. Unsteady Pressure Prediction

Assessment of the CFD enriched piston theory (EPT) and shock-expansion-piston theory (SEP) models is carried out in terms of C_L using a rigid configuration undergoing +/- 30° pitch maneuver at 10 Hz. The initial conditions for the motion are Mach 4 at 85 kft with a zero incidence angle. Note that the fins maintain an undeflected position during the maneuver. The results are shown in Fig. 12. The EPT model provides a noticeable improvement over the SEP model for this unsteady motion.

Downloaded by UNIVERSITY OF MICHIGAN on April 5, 2018 | http://arc.aiaa.org | DOI: 10.2514/6.2017-0182

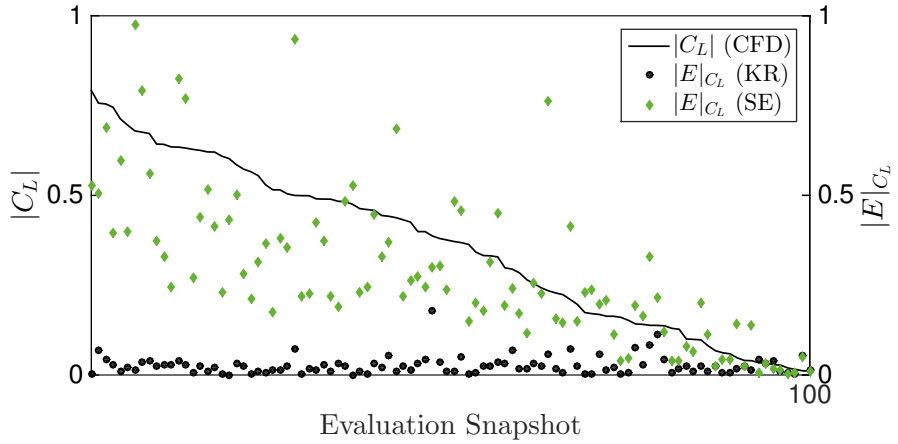

(a) Lift coefficient, C_L

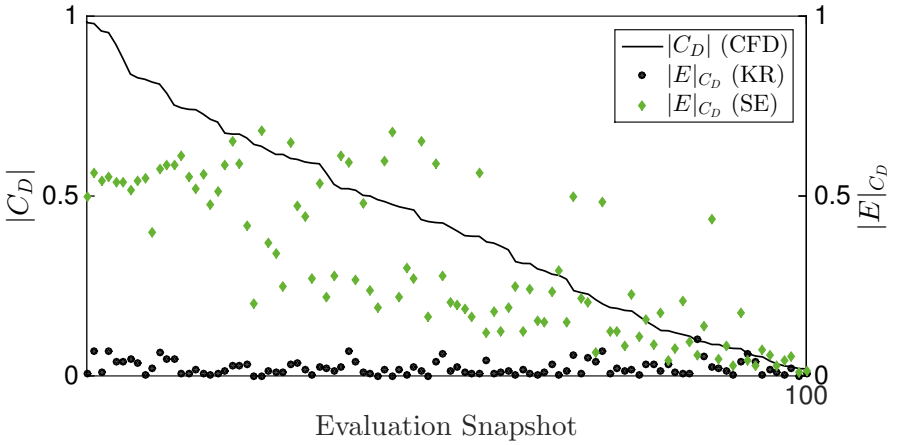

(b) Drag coefficient, C_D

Figure 7. Absolute errors of lift and drag coefficients for Kriging and shock-expansion relative to CFD at evaluation points.

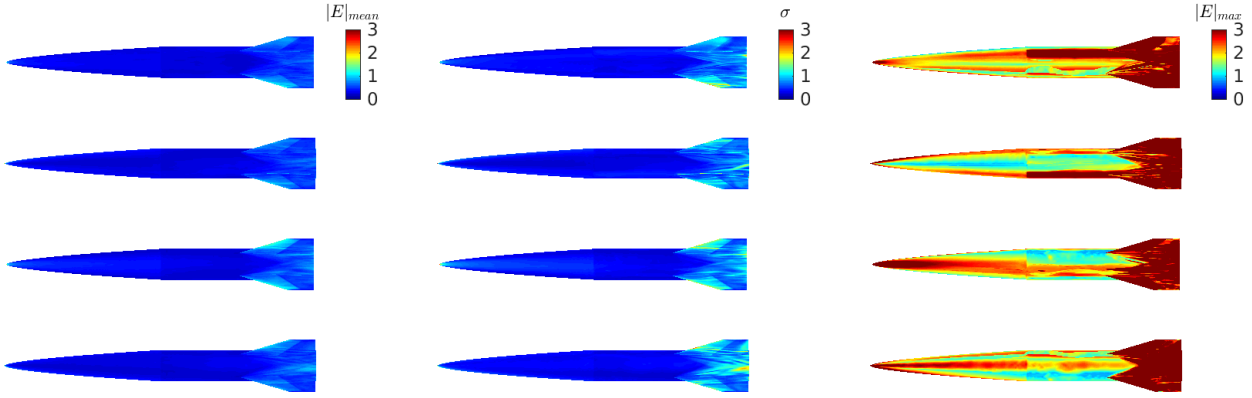

(a) Mean error (b) Standard deviation (c) Max error

Figure 8. Mean and maximum absolute error and standard deviation compared to CFD for Kriging interpolation.

Next, consider the C_L for each of the four fins in Fig. 14, where the fin orientations are denoted in Fig. 13. The predictions for fins 1 and 4, and fins 2 and 3, are nearly identical since the maneuver is comprised of pitch about the y-axis only. The small differences in Kriging predictions for the different pairs of fins is due

Downloaded by UNIVERSITY OF MICHIGAN on April 5, 2018 | http://arc.aiaa.org | DOI: 10.2514/6.2017-0182

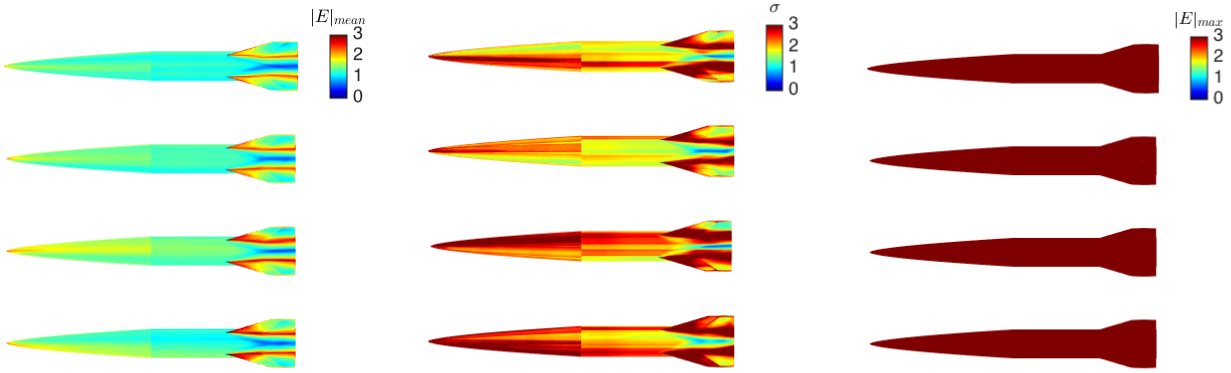

(a) Mean error (b) Standard deviation (c) Max error

Figure 9. Mean and maximum absolute error and standard deviation compared to CFD for the shock-expansion model.

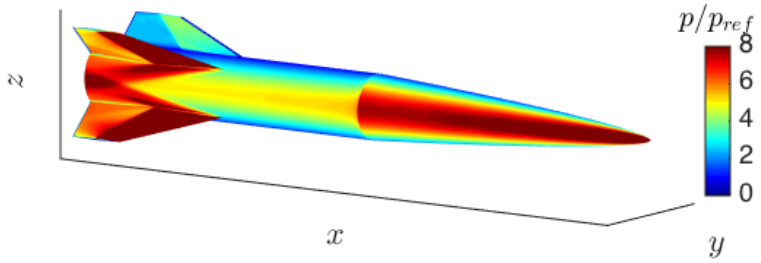

Figure 10. CFD predicted p/p_{ref} at Mach 6.5, 75.8 kft altitude, α = -1.6°, β = 16.7°, and T_w of 594 K.

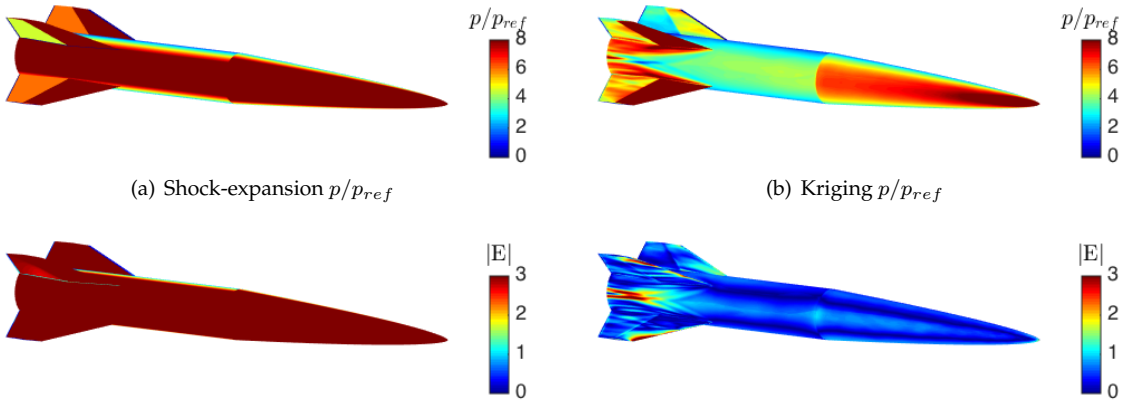

(a) Shock-expansion p/p_{ref} (b) Kriging p/p_{ref}

(c) Shock-expansion absolute error (d) Kriging absolute error

Figure 11. p/p_{ref} and absolute error distributions at Mach 6.5, 75.8 kft altitude, α = -1.6°, β = 16.7°, and T_w of 594 K.

to interpolation error. Similar to the result for the complete geometry in Fig. 12, the EPT prediction for C_L on the fins more closely matches the CFD than the SEP prediction. In particular, note the asymmetry in the CFD prediction about the zero C_L axis. This is due to body-fin flow interactions at higher pitch angles. Again, while SEP is incapable of capturing this effect, Kriging reasonably captures the trend.

Downloaded by UNIVERSITY OF MICHIGAN on April 5, 2018 | http://arc.aiaa.org | DOI: 10.2514/6.2017-0182

Downloaded by UNIVERSITY OF MICHIGAN on April 5, 2018 | http://arc.aiaa.org | DOI: 10.2514/6.2017-0182

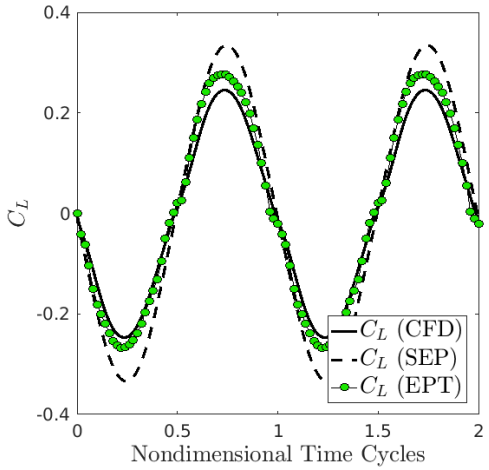

Figure 12. Comparison of C_L predictions for two cycles of a +/-30° pitch maneuver at 10Hz.

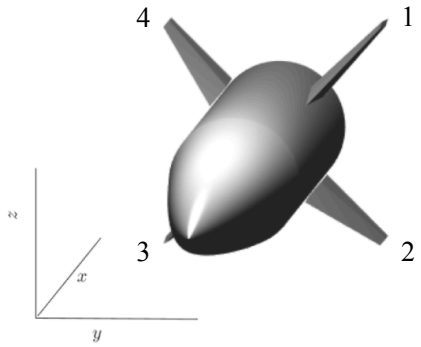

Figure 13. Fin numbering convention.

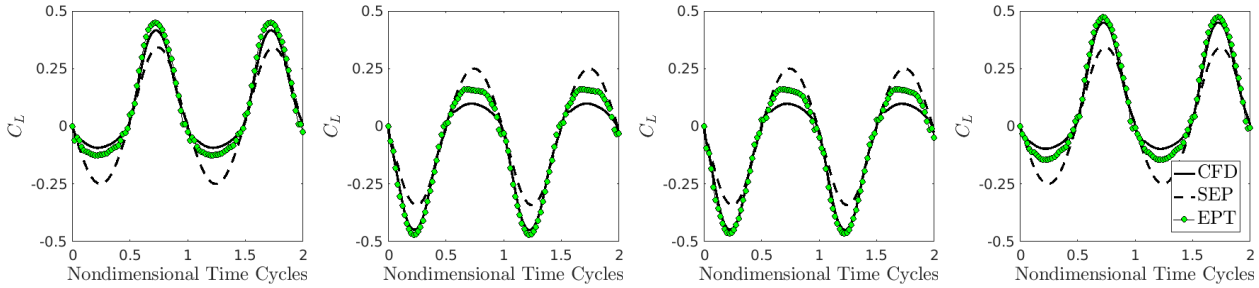

(a) Fin 1 (b) Fin 2 (c) Fin 3 (d) Fin 4

Figure 14. Model comparisons for C_L for two cycles of a +/-30° pitch maneuver at 10 Hz for the fins only.

C. Free Flying Vehicle Response

To compare the impact of the SEP and EPT on vehicle response the following is calculated for each model: 1) trim solution, 2) open loop pitch response, 3) open loop yaw response, and 4) open loop roll response. All open loop simulations began at Mach 6 at 75 kft. The step functions defining the fin deflections for the three maneuvers are listed in Table 5. Note that for each maneuver, any motion in the other planes is restricted in order to isolate the predicted response.

Table 5. Fin deflections for the three isolated maneuvers.

	0 sec $\leq$ time $<$ 1 sec	1 sec $\leq$ time $\leq$ 10 sec
Pitch [Fins 1-4]	[0°, 0°, 0°, 0°]	[+1°, +1°, -1°, -1°]
Yaw [Fins 1-4]	[0°, 0°, 0°, 0°]	[+1°, -1°, -1°, +1°]
Roll [Fins 1-4]	[0°, 0°, 0°, 0°]	[-1°, -1°, -1°, -1°]

1. *Vehicle Trim Comparisons*

The initial conditions to the open loop simulations are established through a trim analysis at a selected cruise condition. Trimming was conducted by minimizing the summed magnitudes of the body forces and moments at Mach 6, 75 kft using the simplex method implemented though the *fminsearch* built-in function in MATLAB.[25] The inputs to the minimization are angle-of-attack, sideslip angle, and all four independent fin deflections. A thrust force equal to the drag plus a weight component is applied along the centerline of the body. Furthermore, the center of gravity is moved 3.556 cm forward from the position listed in Table 2 to match the center-of-pressure location computed using SEP, and thus enforce static stability. A more detailed description of the trimming procedure is provided in [22]; however, in this work, the procedure is expanded to include include lateral, directional, and longitudinal trim.

The trim solutions obtained for SEP and EPT are listed in Table 6 and include the numerical residual of the optimization strategy. Two different trim conditions are considered, namely gravity on and off. When gravity is ignored, the axisymmetric nature of the configuration should result in a trivial trim solution. This is evident when using the SEP model, however there are small deviations needed when using EPT. This is presumably due to interpolation error introduced by the Kriging model. The inclusion of gravity leads to a deviation from the zero trim state for the SEP and an increase in magnitude for the EPT model. However, note symmetry in the fin angles for the SEP model, compared to asymmetry for the EPT fin deflections. This again is an indication of interpolation error introduced by the Kriging model. However, it is evident from these results that the impact of the interpolation error is relatively minor on the trim state. An important issue to note is that the EPT trim solution was observed to be dependent on initial conditions, indicating the presence of local minima. Deeper study into each of these areas is warranted.

Table 6. Trim conditions for SEP and EPT for Mach 6 at 75 kft.

	Gravity off		Gravity on	
	SEP	EPT	SEP	EPT
Angle-of-attack (°)	0.00	0.54	1.20	2.66
Sideslip angle (°)	0.00	-1.04	0.00	-0.83
Fin 1 deflection (°)	0.00	-0.01	0.38	1.20
Fin 2 deflection (°)	0.00	0.65	0.38	2.02
Fin 3 deflection (°)	0.00	0.15	-0.38	-0.99
Fin 4 deflection (°)	0.00	-0.51	-0.38	-1.82
Thrust (N)	1680	1494	1743	1706
Residual	9.10×10^{-13}	1.02×10^{-10}	4.32×10^{-12}	4.71×10^{-8}

2. *Pitch Comparison*

Next, open loop response in pitch is examined by locking directional and lateral degrees of freedom and commanding fin deflection for a positive pitch response as listed in Table 5. Vehicle states θ and q_{ang} using both SEP and EPT are compared in Fig. 15 for cases both with and without the presence of gravity. After one second of trimmed flight, the pitch up fin deflections are commanded, and the SEP model immediately increases the pitch angle more than the EPT model for both cases. This is shown by the magnitude of the

Downloaded by UNIVERSITY OF MICHIGAN on April 5, 2018 | http://arc.aiaa.org | DOI: 10.2514/6.2017-0182

oscillations in Figs. 15(a) & 15(c). The same is true for q_{ang} in Figs. 15(b) & 15(d). When gravity is included, the values of θ after 10 seconds of simulation are closer to one another than when gravity is ignored, while the q_{ang} responses remain similar in both amplitude and frequency.

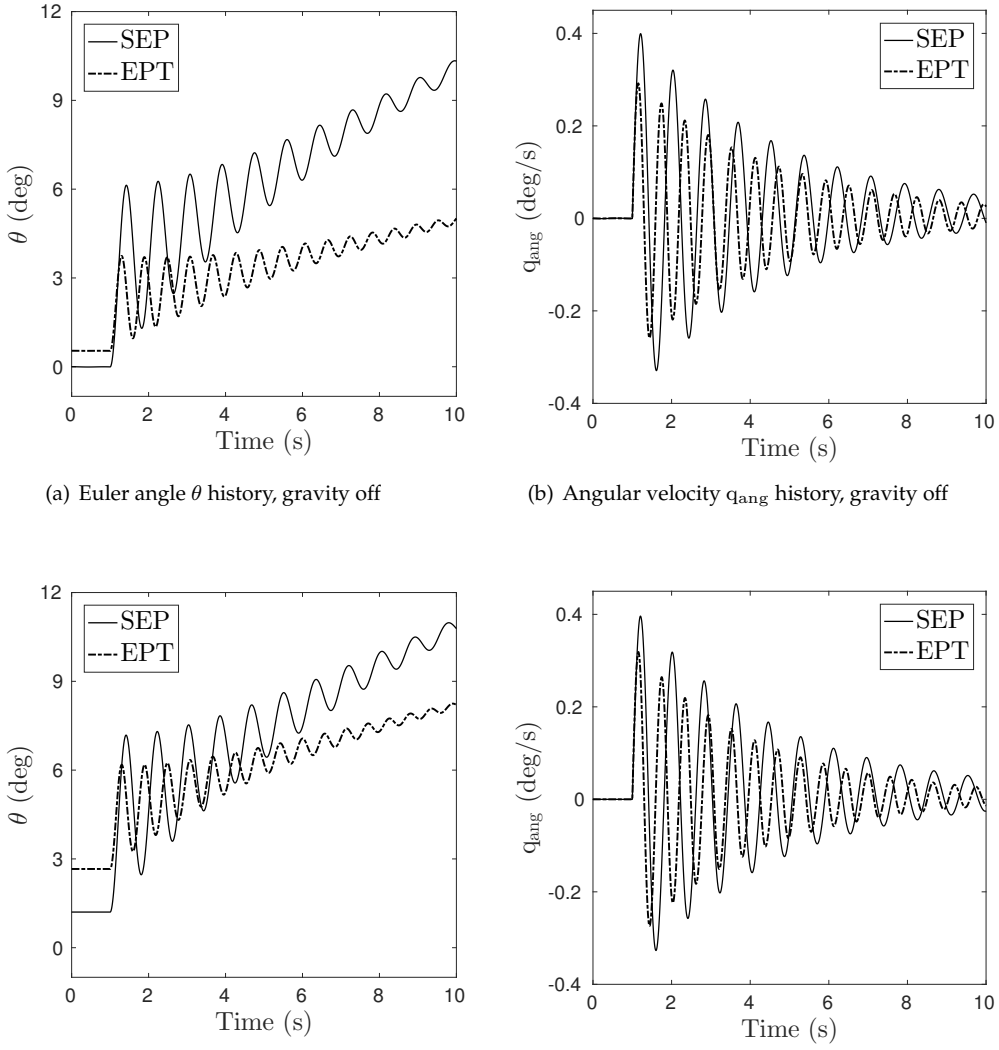

(a) Euler angle θ history, gravity off

(b) Angular velocity q_{ang} history, gravity off

(c) Euler angle θ history, gravity on

(d) Angular velocity q_{ang} history, gravity on

Figure 15. Euler angle θ and angular velocity q_{ang} histories for open loop pitch up simulation.

3. *Yaw Comparison*

Similar to the previous analysis, open loop response in yaw is examined by locking lateral and longitudinal degrees of freedom and commanding fin deflection for a positive yaw maneuver as listed in Table 5. Vehicle states ψ and r_{ang} using both SEP and EPT are compared in Fig. 16 for cases both with and without the presence of gravity. The yaw responses for the two cases shown are similar in both amplitude and frequency. At the onset of the yaw command, SEP predicts a drastically larger change in yaw than EPT. The difference between the two models remains after 10 seconds. The same is true for r_{ang} in Figs. 16(b) & 16(d), despite both models oscillating about zero angular velocity.

Downloaded by UNIVERSITY OF MICHIGAN on April 5, 2018 | http://arc.aiaa.org | DOI: 10.2514/6.2017-0182

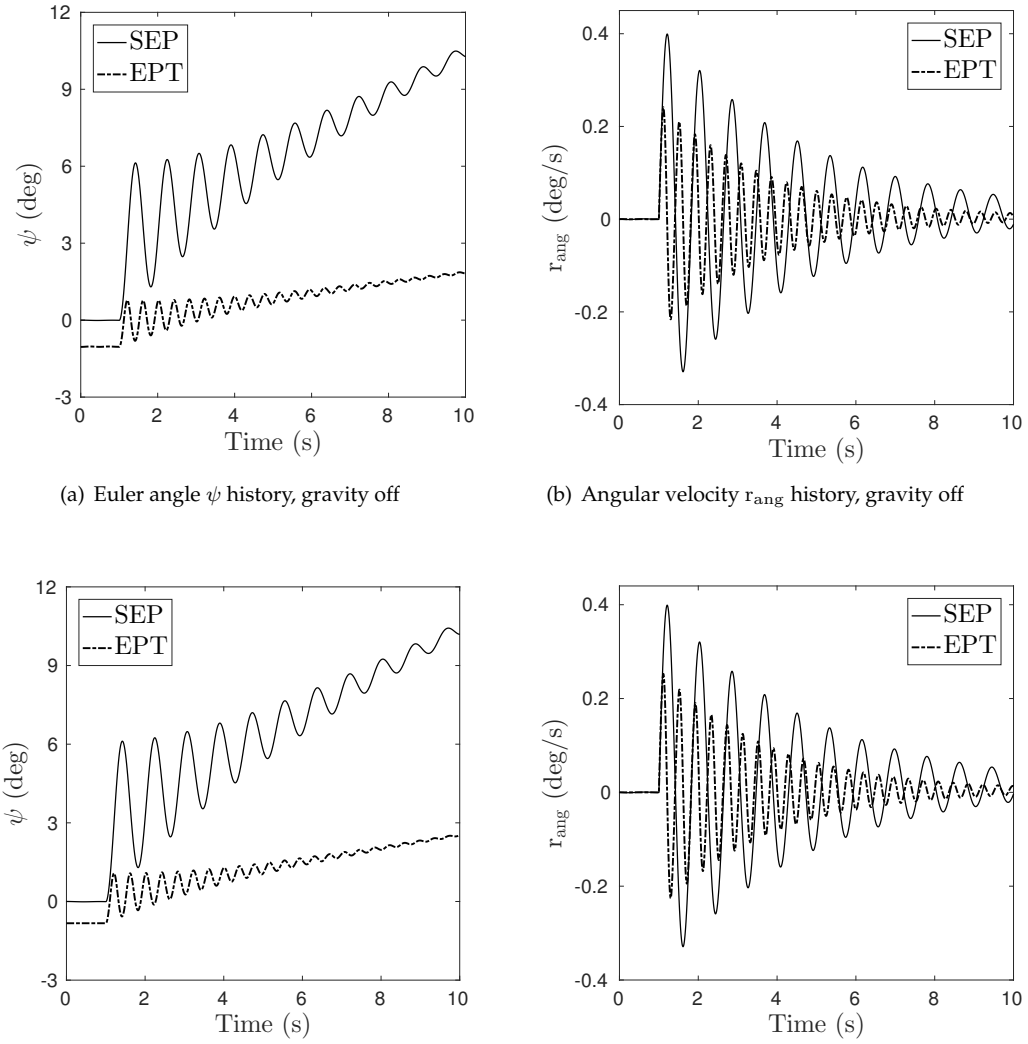

(a) Euler angle ψ history, gravity off

(b) Angular velocity r_{ang} history, gravity off

(c) Euler angle ψ history, gravity on

(d) Angular velocity r_{ang} history, gravity on

Figure 16. Euler angle ψ and angular velocity r_{ang} histories for open loop positive yaw simulation.

Downloaded by UNIVERSITY OF MICHIGAN on April 5, 2018 | http://arc.aiaa.org | DOI: 10.2514/6.2017-0182

4. *Roll Comparison*

Finally, open loop response in roll is examined in the same manner. Similar to the responses for pitch and yaw, the change in roll angle predicted with SEP is larger than when predicted with EPT. This is shown in Fig. 17.

D. Discussion

The above offline results suggest that Kriging interpolation of CFD combined with local piston theory provides significantly improved flow modeling capabilities for maneuvering hypersonic vehicles. Preliminary offline and online results for a maneuvering vehicle indicates that SEP predicts larger magnitudes of response than EPT. However, there are several potential sources of error in the CFD based modeling approach that may influence the preceding analyses. First, interpolation error is found to create unbalanced loads. Second, fin rotation is not presently included in the Kriging model. Thus, aft-body flow interactions, which could be significantly impacted by fin rotation, remain unchanged in the present model. Related to this, the local flow quantities over the fin used for the EPT surface pressure prediction are not updated for fin rotation. This could yield noticeable error in the model predictions at higher fin rotation angles, regardless

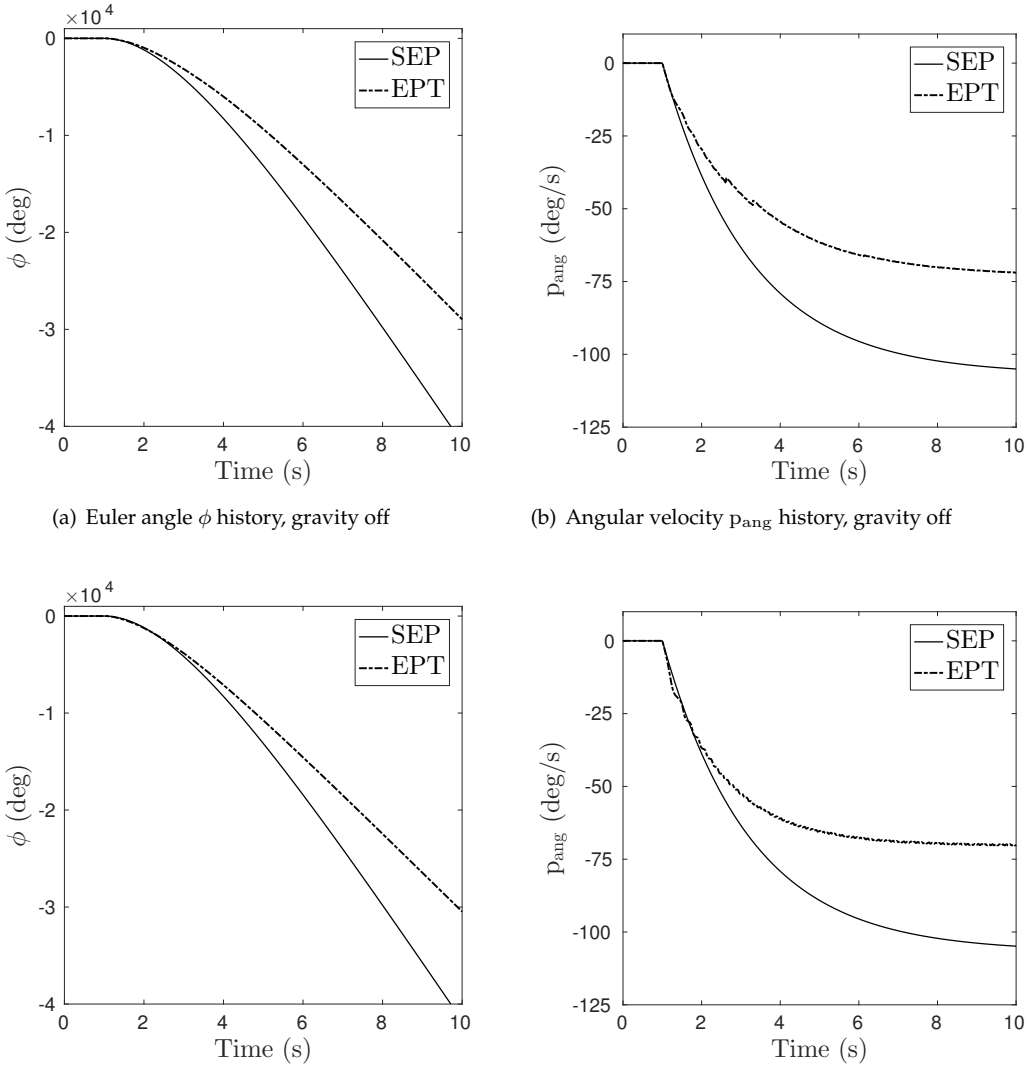

(a) Euler angle ϕ history, gravity off

(b) Angular velocity p_{ang} history, gravity off

(c) Euler angle ϕ history, gravity on

(d) Angular velocity p_{ang} history, gravity on

Figure 17. Euler angle ϕ and angular velocity p_{ang} histories for open loop positive roll simulation.

of any flow interactions that may occur. Finally, the surface grid resolution used in the UM/HSV code is relatively coarse compared to the CFD predictions. This requires mapping of the CFD pressure solutions to the vehicle simulation grid prior to constructing the Kriging model, and an associated potential for loss of information and added interpolation errors. The impact of each of these issues are currently under further investigation.

E. Computational Expense

The computational expenses of the different modeling approaches are listed in Table 7. The computational time to obtain the training data for Kriging model construction is computed using the cost of the steady-state CFD listed in Table 7 multiplied by the number of training points. However, the actual wall time for the generation of the training data is highly dependent on the number of available computer processing cores. Since the generation of the training points is an embarrassingly parallel process, each training point could be generated in parallel provided enough computer processing cores were accessible. For example, on a mid-scale parallel computer system (approx. 50,000 cores), the Kriging training data could be generated in a wall time on the order of 12 hours. As Table 7 demonstrates, once constructed, the CFD enriched

Downloaded by UNIVERSITY OF MICHIGAN on April 5, 2018 | http://arc.aiaa.org | DOI: 10.2514/6.2017-0182

piston theory approach maintains a low computational expense comparable to classical engineering level approximations.

Table 7. Wall times of different modeling approaches.

Method of Pressure Prediction	1 Steady-State Prediction (s)	1 Unsteady Prediction (s)
CFD[a,b]	7.0×10^3	2.0×10^2
CFD Enriched Piston Theory[c]	6.5×10^{-3}	1.6×10^{-2}
Shock-Expansion-Piston Theory[c]	1.1×10^{-3}	1.1×10^{-2}

[a] 2.70 GHz Intel Xeon E5-2697v2 processors (264)

[b] single unsteady iteration not including time for generating initial steady-state solution

[c] 3.70 GHz Intel i3-6100 processors (4)

Downloaded by UNIVERSITY OF MICHIGAN on April 5, 2018 | http://arc.aiaa.org | DOI: 10.2514/6.2017-0182

IV. Concluding Remarks

This work assesses modeling approaches for aerodynamic surface pressure and loads for representative trajectories of a full-scale, 3-D hypersonic vehicle. The unsteady pressure is modeled using a local piston theory approach, where the local flow quantities are provided using either shock-expansion theory or Kriging interpolation of offline steady-state CFD solutions.

The offline accuracy of the pressure models was evaluated for both steady-state and unsteady loads predictions relative to RANS CFD. Kriging interpolation was found to produce significantly improved steady-state aerodynamic load predictions compared to a shock-expansion method. Improvements were observed in terms of 3-D effects and aft-body flow interactions. Furthermore, the CFD enriched piston theory approach was found to provide significantly improved unsteady pressure predictions for both the full vehicle and the individual fins over a prescribed pitch maneuver. In particular, trends in reduction of fin lift due to body-fin flow interactions were obtained with the CFD enriched piston theory approach.

The impact of the two modeling approaches on vehicle dynamics was evaluated by computing trim states and then commanding three isolated maneuvers in a free flying open loop simulation, initialized at the trim states. The Euler angles for the pitch and yaw responses exhibit noticeable differences in both the magnitude of oscillation and angle at the end of 10 seconds. Similarly, the roll results differ in magnitude, and the roll angular velocities differ at the end of 10 seconds. The root causes of this are postulated as a combination of: 1) aft-body flow interactions that are not captured by a shock-expansion-piston theory model, 2) potential modeling errors in the CFD enriched piston theory approach, and 3) over-prediction of the steady-state component in the SEP model. Current efforts are focused on systematically studying this problem using CFD on a vehicle with moving fins.

V. Acknowledgements

The authors gratefully acknowledge funding for this work through the AFRL Cooperative Agreement FA8651-13-2-0007, with Dr. Crystal Pasiliao as Technical monitor, and the AFRL Scholars Program; and also technical insights from Dr. Daniel Reasor (AFRL), Mr. Zachary Witeof (Leidos), Dr. Anton VanderWyst (Leidos), and Mr. Kirk Brouwer (OSU).

References

[1]Witeof, Z. D. and Pasiliao, C. L., "Fluid-Thermal-Structural Interaction Effects in Preliminary Design of High Speed Vehicles," AIAA 2015-1631, 2015.

[2]Falkiewicz, N. J., Cesnik, C. E. S., Crowell, A. R., and McNamara, J. J., "Reduced-Order Aerothermoelastic Framework for Hypersonic Vehicle Control Simulation," *AIAA Journal*, Vol. 49, No. 8, 2011, pp. 1625–1646.

[3]Dowell, E. H. and Hall, K. C., "Modeling of Fluid-Structure Interaction," *Annual Review of Fluid Mechanics*, Vol. 33, No. 1, 2001, pp. 445–490.

[4]Lucia, D. J., Beran, P. S., and Silva, W. A., "Reduced-Order Modeling: New Approaches for Computational Physics," *Progress in*

Aerospace Sciences, Vol. 40, No. 1, 2004, pp. 51–117.

[5]Glaz, B., Liu, L., Friedmann, P. P., Bain, J., and Sankar, L. N., "A Surrogate-Based Approach to Reduced-Order Dynamic Stall Modeling," *Journal of the American Helicopter Society*, Vol. 57, No. 2, 2012, pp. 022002–9.

[6]McNamara, J. J., Crowell, A. R., Friedmann, P. P., Glaz, B., and Gogulapati, A., "Approximate Modeling of Unsteady Aerodynamics for Hypersonic Aeroelasticity," *Journal of Aircraft*, Vol. 47, No. 6, 2010, pp. 1932–1945.

[7]Crowell, A. R., McNamara, J., and Miller, B., "Hypersonic Aerothermoelastic Response Prediction of Skin Panels Using Computational Fluid Dynamic Surrogates," *Journal of Aeroelasticity and Structural Dynamics*, Vol. 2, No. 2, 2011.

[8]Crowell, A. R. and McNamara, J. J., "Model Reduction of Computational Aerothermodynamics for Hypersonic Aerothermoelasticity," *AIAA Journal*, Vol. 50, No. 1, 2012, pp. 74–84.

[9]Crowell, A. R., Miller, B. A., and McNamara, J. J., "Robust and Efficient Treatment of Temperature Feedback in Fluid–Thermal–Structural Analysis," *AIAA Journal*, Vol. 52, No. 11, 2014, pp. 2395–2413.

[10]Brouwer, K., Crowell, A., and McNamara, J., "Rapid Prediction of Unsteady Aeroelastic Loads in Shock-Dominated Flows," AIAA 2015-0687, 2015.

[11]Zettl, D., Dreyer, E. R., Grier, B. J., McNamara, J. J., and Pasiliao, C. L., "Rapid Steady-State Pressure Prediction for Ultra High-Speed Vehicles," AIAA 2016-1323, 2016.

[12]Biedron, R., Derlaga, J., Gnoffo, P., Hammond, D., Jones, W., Kleb, B., Lee-Rausch, E., Nielson, E., Park, M., Rumsey, C., Thomas, J., and Wood, W., *FUN3D Manual: 12.5*, NASA/TM-2014-218520.

[13]Wang, Q., Massey, S. J., Abdol-Hamid, K. S., and Frink, N. T., "Solving Navier-Stokes Equations with Advanced Turbulence Models on Three-Dimensional Unstructured Grids," AIAA 1999-0156, 1999.

[14]Witeof, Zachary D, N. L., "Initial Concept 3.0 Finite Element Model Definition," Rept. AFRL-RWWWV-TN-2014-0013, Eglin AFB, FL, April 2014.

[15]Pasiliao, C. L., Sytsma, M. J., Neergaard, L., Witeof, Z., and Trolier, J. W., "Preliminary Aero-Thermal Structural Simulation," AIAA 2014-2292, 2014.

[16]Oberkampf, W. L. and Roy, C. J., *Verification and Validation in Scientific Computing*, Cambridge University Press, 2010.

[17]Morgan, H. G., "Theoretical considerations of flutter at high Mach numbers," *Journal of the Aerospace Sciences*, 1958.

[18]Lighthill, M. J., "Oscillating Airfoils at High Mach Number," *Journal of the Aeronautical Sciences (Institute of the Aeronautical Sciences)*, Vol. 20, No. 6, 1953.

[19]Zhang, W.-W., Ye, Z.-Y., Zhang, C.-A., and Liu, F., "Supersonic flutter analysis based on a local piston theory," *AIAA Journal*, Vol. 47, No. 10, 2009, pp. 2321–2328.

[20]Anderson, J. D., *Modern Compressible Flow: With Historical Perspective*, McGraw Hill Higher Education, 1990.

[21]Wang, X. and Hickernell, F. J., "Randomized Halton Sequences," *Mathematical and Computer Modelling*, Vol. 32, No. 7, 2000, pp. 887–899.

[22]Klock, R. J. and Cesnik, C. E. S., "Aerothermoelastic Reduced-Order Model of a Hypersonic Vehicle," AIAA 2015-2711, 2015.

[23]Klock, R. J. and Cesnik, C. E. S., "Aerothermoelastic Simulation of Air-Breathing Hypersonic Vehicles," AIAA 2014-0149, 2014.

[24]Falkiewicz, N. J. and Cesnik, C. E. S., "Partitioned Time-Domain Substructure Coupling Methodology for Efficient Hypersonic Vehicle Simulation," *AIAA Journal*, Vol. 53, No. 11, 2015, pp. 3167–3186.

[25]MathWorks Corp., Natick, MA., *Matlab*, ver. 8.1, rel. 2013a ed., 2013.

Downloaded by UNIVERSITY OF MICHIGAN on April 5, 2018 | http://arc.aiaa.org | DOI: 10.2514/6.2017-0182